



Nonisothermal Modeling of Polymer Electrolyte Fuel Cells

I. Experimental Validation

Hyunchul Ju,^a Chao-Yang Wang,^{a,*} Simon Cleghorn,^b and Uwe Beuscher^{b,**}

^aElectrochemical Engine Center and Department of Mechanical and Nuclear Engineering,
The Pennsylvania State University, University Park, Pennsylvania 16802, USA

^bGore Fuel Cell Technologies, W. L. Gore & Associates, Incorporated, Elkton, Maryland 21921, USA

A three-dimensional, nonisothermal model of polymer electrolyte fuel cells (PEFC) is applied to a 50 cm² cell under various humidity conditions and validated against experimental data of current distribution. In low-humidity operation, coupled modeling of water and heat management is essential as the current density distribution is mainly controlled by hydration of the polymer electrolyte, which is a strong function of temperature due to the water vapor saturation pressure increasing exponentially with temperature. Since these validation simulations involve several millions of computational grid points and hence are considered large-scale calculations, a parallel computational methodology has been employed to substantially reduce the computational time and relax the memory requirement. The model predictions compare well with the detailed experimental data over a wide range of humidity conditions at anode and cathode, and furthermore reveal the complex interplay of heat and water transport phenomena inside PEFC through extensive multidimensional contours of species concentration, temperature, and current density.
© 2005 The Electrochemical Society. [DOI: 10.1149/1.1943591] All rights reserved.

Manuscript submitted January 4, 2005; revised manuscript received February 24, 2005. Available electronically July 12, 2005.

Polymer electrolyte fuel cells (PEFC) convert the chemical energy of fuel and oxidant into electrical energy, releasing the balance as heat. In automotive applications, high power density operation is demanded, resulting in more waste heat released, and thus the thermal effect on PEFC performance is critical.

Ju and Wang¹ performed a detailed experimental validation of an isothermal PEFC model using current density distribution data measured under fully humidified inlet conditions. This work clearly demonstrated that validation of multiphysics PEFC models must be performed against distributed fuel cell data. Low-humidity operation is of increasing interest especially for automotive fuel cell applications. In this case, the current density distribution is expected to be mainly controlled by the hydration of the polymer electrolyte membrane, which is a strong function of temperature as the water vapor saturation pressure increases exponentially with temperature. Thus, thermal modeling is required for a detailed validation study under low-humidity conditions. The objective of this work is to validate a model that couples electrochemical reactions, transport phenomena, and thermal effects against detailed data of current distribution in low-humidity conditions, and to elucidate the complex interplay of heat and water management under such conditions.

Thermal modeling of a PEFC starts with the energy equation that balances heat generation from the cell with heat removal. Heat generation in a fuel cell undergoing no phase change includes entropic heat of reactions, the irreversible heat of electrochemical reactions, and Joule heating.² Roughly, the irreversible reaction heat, entropic heat, and Joule heating in a PEFC account for 55, 35, and 10% of total heat release, respectively. The entropic heat, also called reversible heat or Peltier effect,² is the difference between the total chemical energy of reactants and the maximum usable work according to the second law of thermodynamics. The irreversible heat results from the irreversibility of the electrochemical reactions, and the Joule heating is caused by finite resistances of various components used in the PEFC.

A number of PEFC thermal models have been published in the literature.³⁻¹⁵ These ranged from simplified one-dimensional models for individual components and full cells to multiphysics, multidimensional, two-phase computational fuel cell dynamics (CFCD) models. Most recently, Ju et al.¹⁵ developed a rigorous thermal model for PEFC in which the reversible reaction heat, $I[-T(\partial U_o/\partial T)]$, often overlooked in the majority of thermal modeling work in the literature, was included. This term turns out to

be a significant contributor to overall heat generation (>30% of the total heat release). In addition, unambiguous and location-specific heat generation expressions were developed for use in a detailed multidimensional PEFC model that includes gas channels, gas diffusion layers, catalyst layers, and the membrane. Fully three-dimensional simulations were carried out since the primary mechanism of heat removal from the reaction area of the PEFC is by in-plane heat conduction through the GDL to the current collecting ribs, which act as a heat sink. The reader is referred to Ju et al.¹⁵ for a detailed review of nonisothermal PEFC modeling.

In this paper, we apply the three-dimensional, nonisothermal PEFC model of Ju et al.¹⁵ to a 50 cm² segmented cell. The nonisothermal model is validated extensively against various sets of current density distribution data experimentally measured under various cell voltages and inlet humidification conditions. As calculations for a 50 cm² cell require millions of computational cells to be accurate, a parallel computational methodology developed by Meng and Wang¹⁶ is employed to reduce the computational and memory requirements.

Experimental

Model assumptions and description.—The present three-dimensional, nonisothermal, electrochemical-transport coupled model was developed based on the previous works of Gu and Wang¹⁷ and Um et al.¹⁸ A detailed elaboration of the model was given in Ju et al.¹⁵ Here, only a brief overview of the model is given. The PEFC model accounts for heat and mass transport phenomena in all subregions of PEFC: gas channels, diffusion and catalyst layers on both anode and cathode sides, and the ionomeric membrane. The assumptions made in the present model are as follows:

1. ideal gas mixtures;
2. incompressible and laminar flow due to small pressure gradients and flow velocities;
3. negligible ohmic potential drop in the electronically conductive solid matrix of porous diffusion and catalyst layers, as well as in the current collectors due to their relatively very large electrical conductivities; and
4. single-phase flow for water transport (*i.e.*, no liquid water).

Due to assumption 3, the electrode becomes an equipotential line such that

$$\phi_s = 0 \quad \text{for anode}$$

* Electrochemical Society Active Member.

^z E-mail: cwx31@psu.edu

Table I. Single-phase nonisothermal steady-state PEFC model: Governing equations with source terms.

| | Conservation equations | Source terms |
|----------|--|--|
| Mass | $\nabla \cdot (\rho \mathbf{u}) = 0$ | |
| Momentum | $1/\varepsilon^2 \nabla \cdot (\rho \mathbf{u} \mathbf{u}) = -\nabla p + \nabla \cdot \boldsymbol{\tau} + S_u$ | In diffusion and catalyst layers: $S_u = -\mu/Ku$ |
| Species | $\nabla \cdot (\mathbf{u} C_k) = \nabla \cdot (D_k^{\text{eff}} \nabla C_k) + S_k$ | In catalyst layers: $S_k = -s_k j/nF$ |
| Charge | $\nabla \cdot (\kappa^{\text{eff}} \nabla \Phi_e) + S_\Phi = 0$ | For water in catalyst layers: $S_k = -\nabla \cdot (n_d/FI) - s_k j/nF$ |
| Energy | $\nabla \cdot (\rho c_p \mathbf{u} T) = \nabla \cdot (k^{\text{eff}} \nabla T) + S_T$ | In catalyst layers: $S_\Phi = j$ |
| | | In catalyst layers: $S_T = j(\eta + TdU_o/dT) + I^2/\kappa^{\text{eff}}$ |
| | | In membrane: $S_T = I^2/\kappa^{\text{eff}}$ |
| | Electrochemical reaction: $\sum_k s_k M_k^z = ne^-$ | where $\begin{cases} M_k \equiv \text{chemical formula of species } k \\ s_k \equiv \text{stoichiometry coefficient} \\ n \equiv \text{number of electrons transferred} \end{cases}$ |
| | Hydrogen oxidation reaction (HOR) in anode side: Oxygen reduction reaction (ORR) in cathode side: | $\begin{aligned} \text{H}_2 - 2\text{H}^+ &= 2e^- \\ 2\text{H}_2\text{O} - \text{O}_2 - 4\text{H}^+ &= 4e^- \end{aligned}$ |

$$\phi_s = V_{\text{cell}} \quad \text{for cathode}$$

$$U_o = 1.23 - 9.0 \times 10^{-4}(T - 298.15) \quad [4]$$

Assumption 3 also implies that ohmic Joule heating in the current collectors, gas diffusion layers (GDL), and catalyst layers is negligible due to their high electric conductivities. Assumption 4 is valid under the condition that the liquid saturation within the GDL is low, or liquid droplets are small and disperse in gas flow to form a mist flow. Therefore, the single-phase approach is particularly well suited for fuel cell simulations under low-humidity operation. The heat release/absorption due to phase change of water is also excluded because of assumption 4.

Under these assumptions, the PEFC thermal model consists of conservation equations of mass, momentum, chemical species, electric charge, and thermal energy. A single-domain approach is used to make a single set of governing equations valid for all subregions. Thus, no interfacial conditions have to be specified at internal boundaries between the various regions. All the governing equations are summarized in Table I with their respective volumetric source terms identified for various subregions of a fuel cell. Brief comments on each of the five governing equations follow.

In porous regions, superficial velocities are used in order to automatically ensure mass flux continuity at the interface between porous and nonporous regions. The source terms in the momentum equations are devised to recover Darcy's law under the limiting condition where the permeability of the porous medium is small and hence the velocity is small.

The source term in the charge equation is used to describe the generated current between the solid matrix and the electrolyte phase inside each of anode and cathode catalyst layers. The transfer current densities are expressed as follows

$$j = ai_{0,a}^{\text{ref}} \left(\frac{C_{\text{H}_2}}{C_{\text{H}_2,\text{ref}}} \right)^{1/2} \left(\frac{\alpha_a + \alpha_c}{RT} \times F \times \eta \right) \quad \text{for anode} \quad [1]$$

$$j = -ai_{0,c}^{\text{ref}} \left(\frac{C_{\text{O}_2}}{C_{\text{O}_2,\text{ref}}} \right) \exp \left(-\frac{\alpha_c}{RT} \times F \times \eta \right) \quad \text{for cathode} \quad [2]$$

The kinetic expressions representing the hydrogen oxidation reaction (HOR) in the anode catalyst layer and oxygen reduction reaction (ORR) in the cathode catalyst layer are simplified from the general Butler-Volmer kinetics because the HOR kinetic is facile and the ORR kinetic is slow.¹ The surface overpotential, η , for the HOR and ORR reactions, is defined as

$$\eta = \phi_s - \phi_e - U_o \quad [3]$$

where the thermodynamic equilibrium potential, U_o , is the equilibrium potential for a H₂/air fuel cell. It is calculated from thermodynamic data of reaction enthalpy and entropy changes and is assumed to be zero for the anode but a function of temperature for the cathode as follows¹⁹

The temperature dependence of the ORR exchange current density can be expressed in Arrhenius form as follows

$$ai_{0,c}^{\text{ref}}(T) = ai_{0,c}^{\text{ref}}(353\text{K}) \times \exp \left[-\frac{E_a}{R} \left(\frac{1}{T} - \frac{1}{353.15} \right) \right] \quad [5]$$

where E_a denotes the activation energy for oxygen reduction at the Pt/Nafion electrode as provided by Parthasarathy et al.²⁰ and herein listed in Table IV.

The source terms in the species equations represent the production or consumption of species k by the electrochemical reactions (*i.e.*, anode HOR and cathode ORR) and the water transport from the anode through the membrane to the cathode by the electro-osmotic drag effect. The mass diffusion coefficient of species k , D_k , in the anode and cathode gas channels is obtained from Bird et al.²¹ as a function of temperature and pressure. For the porous regions of a PEFC such as the gas diffusion and catalyst layers, the expression is modified into effective transport properties to account for the effects of porosity and tortuosity in the porous regions as follows

$$D_k = D_0 \left(\frac{T}{T_0} \right)^{3/2} \left(\frac{P_0}{P} \right) \quad \text{for gas channels} \quad [6]$$

$$D_k^{\text{eff}} = \frac{\varepsilon}{\tau} \times D_k \quad \text{for porous regions} \quad [7]$$

where ε and τ are the porosity and tortuosity of the porous medium, respectively.

The three heat source terms in the energy equation deserve special attention. They represent irreversible heat of the electrochemical reaction, reversible entropic heat, and Joule heating, respectively. Gu and Wang¹⁷ provided the location-specific expressions for these terms as used in Table I. In addition, the heat accumulation in a porous material consisting of the matrix and fluid is given by

$$\rho c_p = \varepsilon(\rho c_p)_f + (1 - \varepsilon) \times (\rho c_p)_s \quad \text{for porous regions} \quad [8]$$

where the heat capacitance (ρc_p) with subscripts "f" and "s" is referred to the fluid and the solid matrix, respectively.

The transport properties of electrolytes are given by Springer et al.,²² where the electro-osmotic drag coefficient for water, n_d , the water diffusivity, $D_{w,\text{mem}}$, and the proton conductivity, κ_{mem} , in the membrane are correlated with the water content of the membrane, λ , which in turn a function of the water activity, a , as follows

$$a = \frac{C_w^g RT}{P^{\text{sat}}} \quad [9]$$

$$\lambda = \begin{cases} 0.043 + 17.81a - 39.85a^2 + 36.0a^3 & \text{for } 0 < a \leq 1 \\ 14 + 1.4(a - 1) & \text{for } 1 < a \leq 3 \end{cases} \quad [10]$$

$$n_d = \frac{2.5\lambda}{22} \quad [11]$$

$$\kappa_{\text{mem}} = (0.5139\lambda - 0.326)\exp\left[1268\left(\frac{1}{303} - \frac{1}{T}\right)\right] \quad [12]$$

$$D_{w,\text{mem}} = \begin{cases} 2.692661843 \times 10^{-10} & \text{for } \lambda \leq 2 \\ \{0.87(3 - \lambda) + 2.95(\lambda - 2)\} \times 10^{-10} \times e^{[7.9728 - (2416/T)]} & \text{for } 2 < \lambda \leq 3 \\ \{2.95(4 - \lambda) + 1.642454(\lambda - 3)\} \times 10^{-10} \times e^{[7.9728 - (2416/T)]} & \text{for } 3 < \lambda \leq 4 \\ (2.563 - 0.33\lambda + 0.0264\lambda^2 - 0.000671\lambda^3) \times 10^{-10} \times e^{[7.9728 - (2416/T)]} & \text{for } \lambda > 4 \end{cases} \quad [13]$$

In the present work, we choose GORE-SELECT membrane in both experimental and numerical studies, which is a microscopically reinforced composite membrane. Due to the reinforcement, the proton conductivity and water diffusivity had to be adjusted for this study to approximately half of the value of an un-reinforced membrane. Hence, it follows that

$$\kappa_{\text{mem}}^{\text{eff}} = \frac{1}{2} \times \kappa_{\text{mem}} = \frac{1}{2} \times (0.5139\lambda - 0.326)\exp\left[1268\left(\frac{1}{303} - \frac{1}{T}\right)\right] \quad [14]$$

$$D_{w,\text{mem}}^{\text{eff}} = \frac{1}{2} D_{w,\text{mem}} \quad [15]$$

However, an ionomer solution is still used as the electrolyte in the anode and cathode catalyst layers. Consequently, the effective proton conductivity of the anode and cathode catalyst layers follows that of a bulk membrane but with a Bruggmann correction.²³ That is

$$\kappa_{\text{cat}}^{\text{eff}} = \varepsilon_{\text{mc}}^{1.5} \times \kappa_{\text{mem}} \quad [16]$$

where ε_{mc} is the volume fraction of ionomer in the anode and cathode catalyst layers.

Once the electrolyte phase potential, ϕ_e , and the proton conductivity on the membrane, $\kappa_{\text{mem}}^{\text{eff}}$, are obtained, the local current density, I , can be calculated by

$$I = -\kappa_{\text{mem}}^{\text{eff}} \nabla \phi_e \quad [17]$$

The average current density can be obtained by taking the surface average of local current density over the entire membrane

$$I_{\text{avg}} = \frac{1}{A_{\text{mem}}} \int_{A_{\text{mem}}} I dA \quad [18]$$

Boundary conditions.—Equations in Table I form a complete set of governing equations for seven unknowns: \mathbf{u} , p , T , C_{H_2} , C_{O_2} , C_w , and ϕ_e . By use of the single-domain approach, the boundary conditions are required only at the external surfaces of the computational domain. For mass flow, the no-slip and impermeability conditions are applied to all external surfaces except for the inlets and outlets of the anode/cathode gas channels. The inlet species concentrations, $c_{k,\text{in}}$, at the anode/cathode inlet regions are determined by the inlet pressure and humidification conditions. The anode/cathode inlet velocities can be calculated by their respective stoichiometric flow ratios, ζ_a and ζ_c , which are defined as the ratio of the amount of reactant supplied to the amount of reactant required by the electrochemical reaction to generate the overall current density, I_{avg}

$$V_{a,\text{in}} = \zeta_a \times \frac{I_{\text{avg}}}{2F \times C_{\text{H}_2,\text{in}}} \times \frac{A_{\text{mem}}}{A_{a,\text{in}}} \quad [19]$$

$$V_{c,\text{in}} = \zeta_c \times \frac{I_{\text{avg}}}{4F \times C_{\text{O}_2,\text{in}}} \times \frac{A_{\text{mem}}}{A_{c,\text{in}}} \quad [20]$$

Therefore, this approach requires that the cell voltage is iterated until the resulting overall current density is matched with the prescribed value by running a number of whole cell simulations. The outlet species and velocity conditions are the fully developed ones, *i.e.*, the gradient of each variable is zero. For thermal boundary

conditions, the constant temperature condition is applied to the external surfaces of the fuel cell model, since the temperatures of the external surfaces were controlled during the experiments.^{24,25}

Numerical implementation and parallel computation.—The PEFC thermal model described above is implemented into a commercial computational fluid dynamics (CFD) package, STAR-CD, based on its user-coding capability.²⁶ For the detailed validation study, a numerical mesh is generated for the 50 cm² experimental cell with a single-path serpentine flow field as shown in Fig. 1. The long flow path in the serpentine flow field results in a relatively large pressure drop from the inlet to outlet, which may lead to reactant by-pass through the GDL. In the present work, the computational domain of a PEFC consists of the nine subregions, namely gas channels, macro- and micro- gas diffusion layers (GDL), and catalyst layers in both anode and cathode sides, and membrane. All relevant dimensions for the flow field and the other sub-regions are shown in Fig. 1 and Table II, respectively. Based on the grid-independence study by Meng and Wang,¹⁶ roughly 2.3 million computational cells are applied to this fuel cell geometry as shown in Fig. 2. This nonisothermal PEFC model with 2.3 million cells requires about

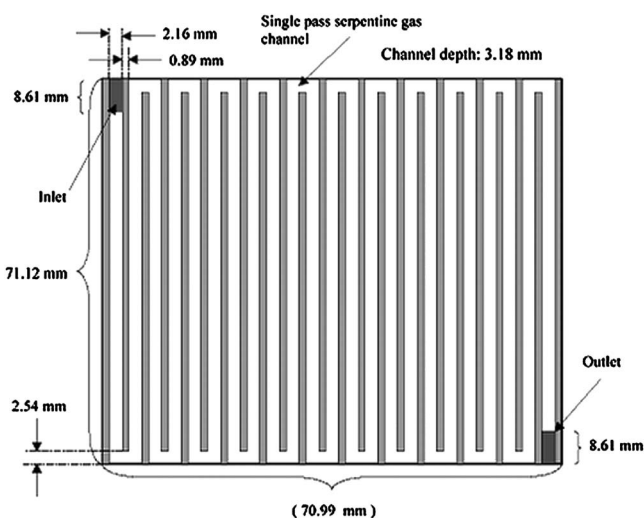


Figure 1. Schematic diagram of the 50 cm² instrumented test cell with relevant dimensions of flow field.

Table II. Cell design parameters.

| Description | Value |
|---|-----------------------------------|
| Anode/cathode macro gas diffusion layers width | 0.175 mm |
| Anode/cathode micro gas diffusion layers width | 0.060 mm |
| Anode/cathode catalyst layers width | 0.010 mm |
| Membrane width (Gore-select) | 0.018 mm |
| Porosity of anode/cathode macro gas diffusion layers, ϵ_{mac} | 0.7 |
| Porosity of anode/cathode micro gas diffusion layers, ϵ_{mic} | 0.5 |
| Porosity of anode/cathode catalyst layers, ϵ_c | 0.6 |
| Tortuosity of porous layers, τ | 5.0 |
| Volume fraction of ionomer in anode/cathode catalyst layers, ϵ_{mc} | 0.26 |
| Permeability of anode/cathode macro gas diffusion layers, K_{mac} | $6.0 \times 10^{-12} \text{ m}^2$ |
| Permeability of anode/cathode micro gas diffusion layers, K_{mic} | $2.0 \times 10^{-15} \text{ m}^2$ |

488 s per iteration on a single PC (2 GHz) and 101 s on a 10-PC cluster (1.4 GHz). More details of the parallel computing methodology can be found in the previous papers.^{1,16}

Results and Discussion

Model validation.—The experiments were performed by Dong et al.²⁵ in a segmented 50 cm² cell using a multichannel potentiostat. The membrane-electrode assembly (MEA) based on a 18 μm thick GORE-SELECT membrane was not segmented, in order to preserve true fuel cell operational characteristics and avoid highly individual specialty membranes. Current density distribution measurements were made under seven different inlet relative humidity (RH) cases. These cases are listed in Table III, based on 80°C cell temperature. For all experimental cases, inlet pressure on both anode and cathode was 3.18 atm, and the anode and cathode stoichiometry ratios were set to be 1.2 and 2.0, respectively. In addition, the temperatures of all external surfaces were maintained at 80°C during the experiments, allowing application of the isothermal boundary condition in the model. The reader is referred to Dong et al.²⁵ for other details of the experiments.

The present nonisothermal PEFC model was extensively validated against the current density distribution data measured under the various inlet humidification and cell voltage conditions. For this validation work, the cathode exchange current density, $i_{0,c}^{\text{ref}}$, the tortuosity of porous layer, τ , and a contact resistance are considered as adjustable parameters. The values of the cathode exchange current density and tortuosity used for all simulation cases are 20 000 A/m³ and 5, respectively. A contact resistance of 150 m Ω cm² is applied in all numerical simulations to account for

Table III. Anode/cathode inlet humidification conditions in various cases.

| Condition number | Case 1 | Case 2 | Case 3 | Case 4 | Case 5 | Case 6 | Case 7 |
|------------------|--------|--------|--------|--------|--------|--------|--------|
| Anode | 50% | 75% | 100% | 0% | 0% | 25% | 100% |
| Cathode | 0% | 0% | 0% | 50% | 100% | 25% | 100% |

all interfacial resistances within the instrumented fuel cell, *e.g.*, at the interface between the catalyst coated membrane (CCM) and GDL and the contact between GDL and current collector land. The use of relatively higher total contact resistance value than that in state-of-the-art single cells is ascribed to the nature of the segmented cell, which exhibits much higher electrical contact resistance between the segmented flow field and GDL. All properties used in the simulations are listed in Table IV.

Figure 3 shows a comparison of simulated and measured current density profiles at cell potentials of 0.85, 0.75, and 0.7 V with an anode and cathode RH of 75 and 0%, respectively (case 2). This is considered a baseline case typical of automotive operation.²⁷ With good agreement between the experimental data and simulation results, both display the characteristics of a low-humidity operation. The current density initially increases as the dry membrane gains moisture from product water and then decreases towards the cathode outlet as oxygen depletion becomes severe and dominates cell performance. Therefore, there is a maximum in the current density distribution and the location of its peak seen in Fig. 3 is indicative of a well-hydrated membrane. It is seen that the current density peaks predicted by the present model remain nearly unchanged at roughly the first 70% of the cell, in consistency with the theoretical expectation that gas reaches full humidification roughly at the same fractional distance under stoichiometry control for all cell voltages or current densities. In contrast, it is seen that the peaks in the experimental data appear in a range of the dimensionless locations. Once the proton conductivity of the membrane reaches the fully saturated value, the current density distribution is controlled by oxygen transport. The competing effects between membrane hydration and oxygen depletion on the current density distribution will be discussed in detail later in this paper.

Figure 4 shows a comparison of simulated and measured current density profiles for case 1 (RH_a/RH_c = 50%/0%) and case 3 (RH_a/RH_c = 100%/0%) at a single voltage of 0.7 V. It can be seen that, in general, the current density distributions match well between simulations and experiments, although there are outlier points near the inlet and outlet. The anode humidification effect is clearly seen in Fig. 4. The current density for 100% anode RH (case 3) is higher

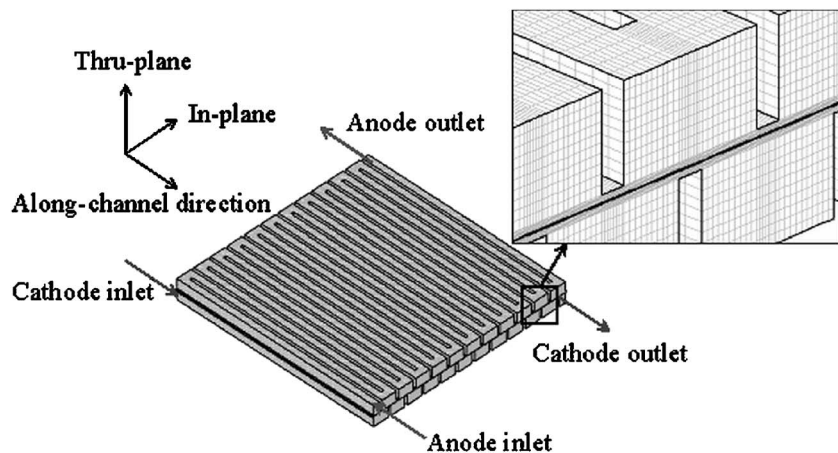


Figure 2. Mesh configuration of the numerical PEFC numerical model with 23-channel serpentine flow field.

Table IV. Kinetics, physical, transport and thermal properties.

| Description | Value |
|--|---|
| Exchange current density \times ratio of reaction surface to catalyst layer volume in anode side, $ai_{0,a}^{ref}$ | 1.0×10^9 A/m ³ |
| Exchange current density \times ratio of reaction surface to catalyst layer volume in cathode side, $ai_{0,c}^{ref}$ | 2.0×10^4 A/m ³ |
| Activation energy for oxygen reduction reaction in cathode side, E_a | 73 269 J/mol |
| Reference hydrogen molar concentration, $c_{H_2,ref}$ | 40.88 mol/m ³ |
| Reference oxygen molar concentration, $c_{O_2,ref}$ | 40.88 mol/m ³ |
| Anodic and cathodic transfer coefficients for hydrogen oxidation reaction | $\alpha_a = \alpha_c = 1$ |
| Cathodic transfer coefficient for oxygen reduction reaction | $\alpha_c = 1$ |
| Dry membrane density, $\rho_{dry,mem}$ | 2000 kg/m ³ |
| Equivalent weight of electrolyte in membrane, EW | 1.1 kg/mol |
| Faraday constant, F | 96487 C/mol |
| Universal gas constant, R | 8.314 J/mol K |
| H ₂ diffusivity in membrane, $D_{H_2}^e$ | 2.59×10^{-10} m ² /s |
| O ₂ diffusivity in membrane, $D_{O_2}^e$ | 1.22×10^{-10} m ² /s |
| H ₂ diffusivity in the anode gas channel, $D_{0,H_2,a}$ | 1.1028×10^{-4} m ² /s |
| H ₂ O diffusivity in the anode gas channel, $D_{0,w,a}$ | 1.1028×10^{-4} m ² /s |
| O ₂ diffusivity in the cathode gas channel, $D_{0,O_2,c}$ | 3.2348×10^{-5} m ² /s |
| H ₂ O diffusivity in the cathode gas channel, $D_{0,w,c}$ | 7.35×10^{-5} m ² /s |
| Thermal conductivity of hydrogen (H ₂), k_{H_2} | 0.2040 W/mK |
| Thermal conductivity of oxygen (O ₂), k_{O_2} | 0.0296 W/mK |
| Thermal conductivity of water vapor, k_w | 0.0237 W/mK |
| Thermal conductivity of nitrogen (N ₂), k_{N_2} | 0.0293 W/mK |
| Thermal conductivity of membrane, k_{mem} | 0.950 W/mK |
| Thermal conductivity of gas diffusion layer, k_{GDL} | 1.5 W/mK |

than that of case 1 (50% anode RH) in roughly the first 70% of the fuel cell, indicating that the higher anode RH helps to retain water in the membrane.

Figure 5 shows the validation results for case 4 at 0.85, 0.75, and

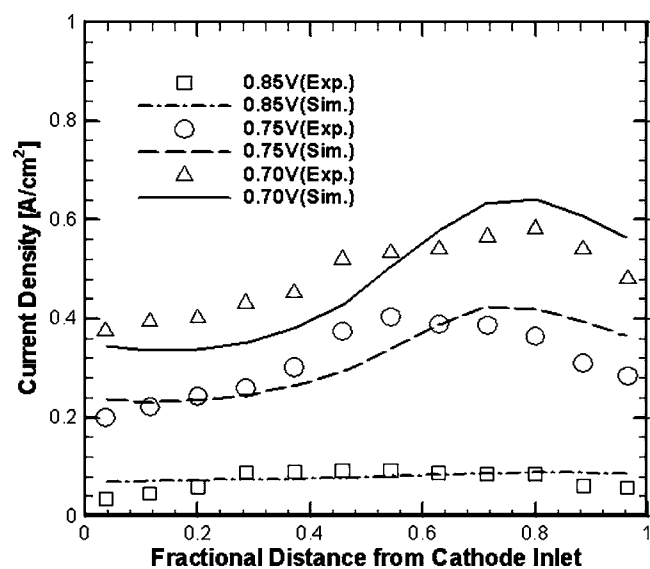


Figure 3. Comparison of simulated (lines) and measured (symbols) current density distributions for case 2: $RH_a/RH_c = 75\%/10\%$ at 80°C.

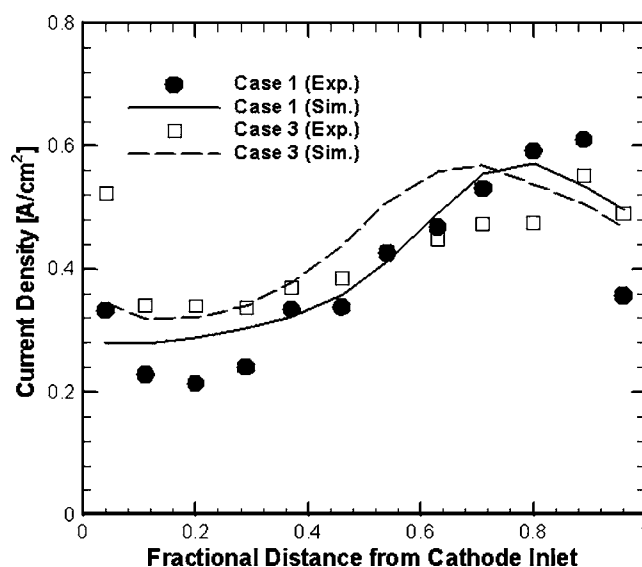


Figure 4. Comparison of simulated (lines) and measured (symbols) current density distributions for case 1 and case 3 at $V_{cell} = 0.7$ V.

0.7 V, where the cathode inlet is partially humidified while the anode inlet is kept dry. Again, good agreement between the simulations and experiments is seen, although there is some scatter in the experimental data. Typical characteristics of low-humidity operation can also be seen similar to Fig. 3 and 4. However, notice that the current density peaks occur earlier within the cell when the cathode is humidified compared to when the anode is humidified (cases 1 through 3). Due to the higher gas flow rate in the cathode than the anode, the same RH in the cathode results in a larger amount of water introduced into the cell compared to the anode. The higher flow rate in the cathode results from the fact that air instead of pure oxygen is fed into the cathode and the cathode stoichiometry is higher than the anode. Consequently, approximately in the first half of the cell, the current density distributions of case 4 are determined by hydration of the membrane and then controlled by oxygen transport in the second half.

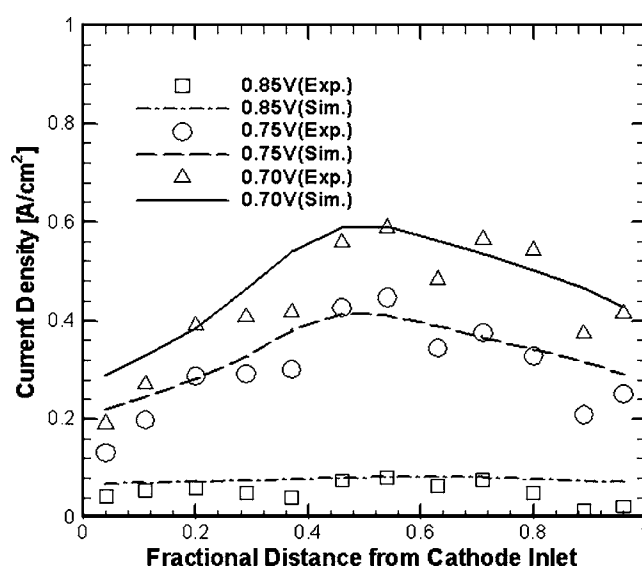


Figure 5. Comparison of simulated (lines) and measured (symbols) current density distributions for case 4: $RH_a/RH_c = 0\%/50\%$ at 80°C.

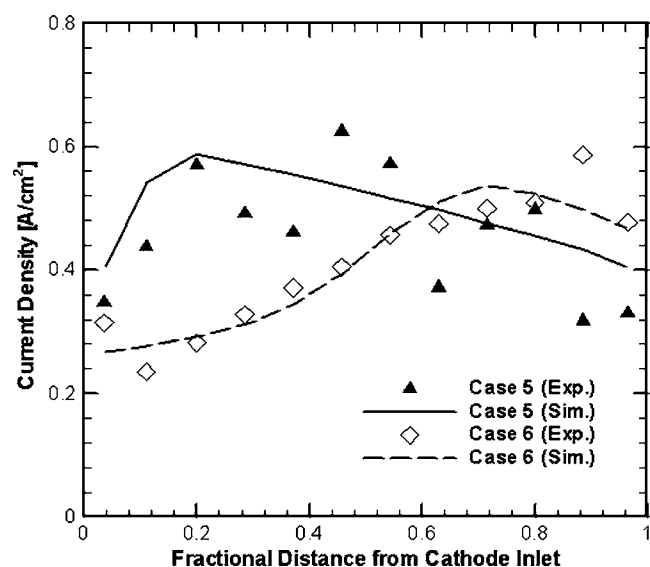


Figure 6. Comparison of simulated (lines) and measured (symbols) current density distributions for case 5 and case 6 at $V_{\text{cell}} = 0.7$ V.

Figure 6 shows the results for case 5 ($RH_a/RH_c = 0\%/100\%$) and case 6 ($RH_a/RH_c = 25\%/25\%$) at 0.7 V. Once again, these cases demonstrate general agreement in the current distributions between the simulations and experiments, although a wider scattering of the experimental data can be observed, particularly in case 5. The cathode humidification effect can be assessed by comparing case 5 ($RH_a/RH_c = 0\%/100\%$) in Fig. 6 with case 4 ($RH_a/RH_c = 0\%/50\%$) at 0.7 V in Fig. 5. The current density peak of case 5 occurs near the inlet due to the higher cathode inlet humidity.

The last validation results, for case 7 ($RH_a/RH_c = 100\%/100\%$), at 0.85, 0.75, and 0.7 V are presented in Fig. 7, where the anode and cathode are both fully humidified at 80°C. Under the fully humidified condition, oxygen depletion is the sole factor to determine the current density distribution and thus, the current densities continue to decrease toward the cathode outlet as shown in Fig. 7. The agreement is relatively poor at 0.7 V, where the experimental data show clear increasing and decreasing trends in the first half of the cell,

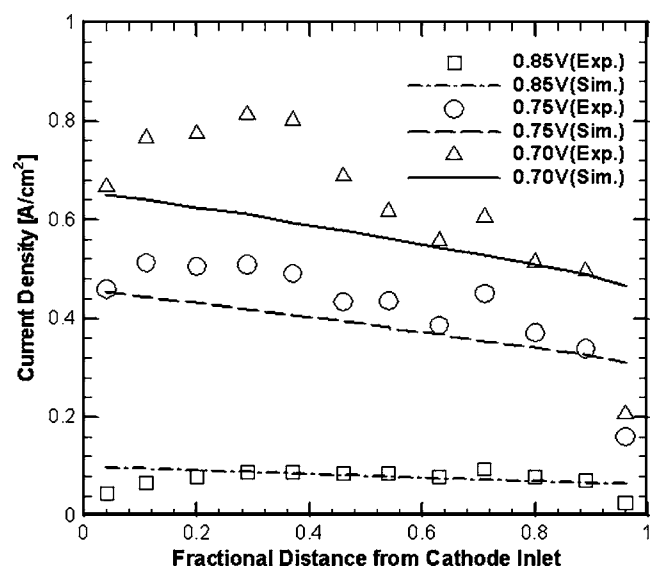


Figure 7. Comparison of simulated (lines) and measured (symbols) current density distributions for case 7: $RH_a/RH_c = 100\%/100\%$ at 80°C.

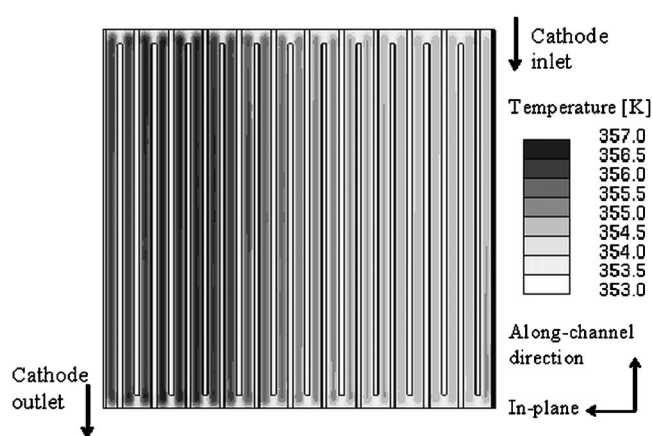


Figure 8. Temperature distribution over the membrane for case 2: $RH_a/RH_c = 75\%/0\%$ and $V_{\text{cell}} = 0.7$ V.

while the simulation continues to show only the oxygen depletion effect. This deviation may be attributed to flooding by liquid water, which may be severe at the fully humidified inlet condition and low cell voltage. The flooding effect cannot be addressed by the present single-phase model. Future work is needed to improve the agreement between experimental data and simulation using a two-phase, nonisothermal model.

Besides the predicted and measured current density profiles along the flow path, multidimensional distributions of species concentration, temperature, and current density are also obtainable from the simulations and should provide greater insight into the low-humidity operation of PEFC. Figure 8 displays the contours of temperature distribution over the membrane for case 2 at 0.7 V. As mentioned earlier, heat generated in the catalyst layer is primarily removed through the GDL to the current collector rib by lateral conduction. As a result, the membrane temperature in the channel region is higher than under the rib. The water activity distribution at the membrane surface for case 2 at 0.7 V is presented in Fig. 9. Due to the temperature distribution shown in Fig. 8 and the fact that the ribs protect the membrane from losing water by mass transport, the water activity of the membrane under the ribs is higher than under the channels. Consequently, even under the low-humidity condition, the water activity near the outlet, particularly under the ribs, becomes greater than unity, implying that the flooding effect is more severe under the ribs than under the channels. Figure 10 is the view of current distribution for case 2 at 0.7 V. Compared with Fig. 9, it is clearly shown that the current density in the channel region is

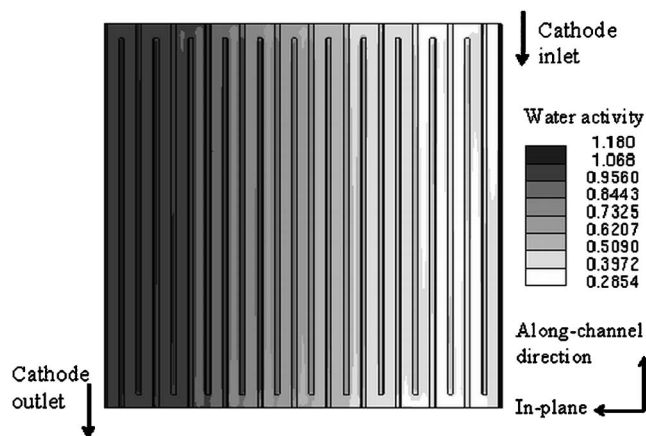


Figure 9. Water activity distribution over the membrane for case 2: $RH_a/RH_c = 75\%/0\%$ and $V_{\text{cell}} = 0.7$ V.

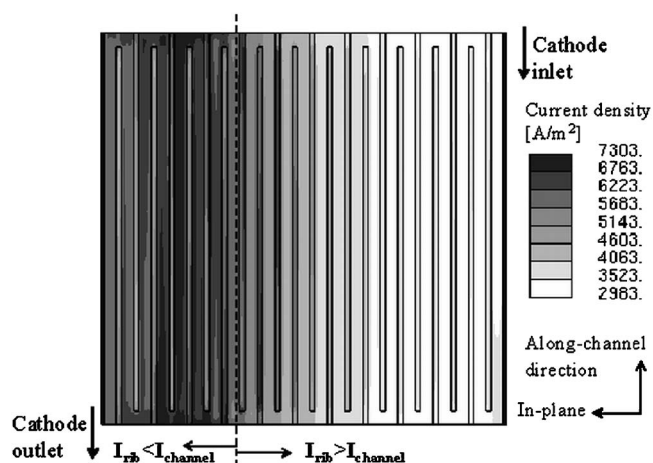


Figure 10. Current density distribution over the membrane for case 2: $RH_a/RH_c = 75\%/0\%$ and $V_{cell} = 0.7$ V.

lower than in the rib region before the membrane becomes fully hydrated. However, the local current density exhibits the opposite trend once the membrane is nearly fully hydrated; hence, the current density begins to be controlled by oxygen transport. The boundary between these two regions (*i.e.*, $I_{rib} > I_{channel}$ and $I_{rib} < I_{channel}$) is denoted by a dashed line in Fig. 10.

The cross-sectional temperature profile along the center line of membrane in the cross section cutting through the middle of the cell for case 2 at 0.7 V is presented in Fig. 11, where the upper and lower bounds correspond to the channel and rib regions, respectively. Consistent with the temperature contour plot (Fig. 8), the spatially fluctuating membrane temperature between channel and rib is caused by a lack of effective cooling in the channel region. In addition, as shown in Table I, all heat generation sources are proportional to the current density. As a result, the temperature bounds increase along the cathode flow path and then decrease near the outlets, following the current density distribution shown in Fig. 3 and 12.

Figure 12 displays calculation results of the current and water activity profiles in the same cross section cutting through the middle of the cell in the same case (case 2, 0.7 V). First, it is clearly shown that the current density increases until the water activity is close to unity and then decreases by oxygen depletion effects, showing that the location of current density peak is indicative of fully hydrated membrane, as mentioned earlier. In addition, the membrane water

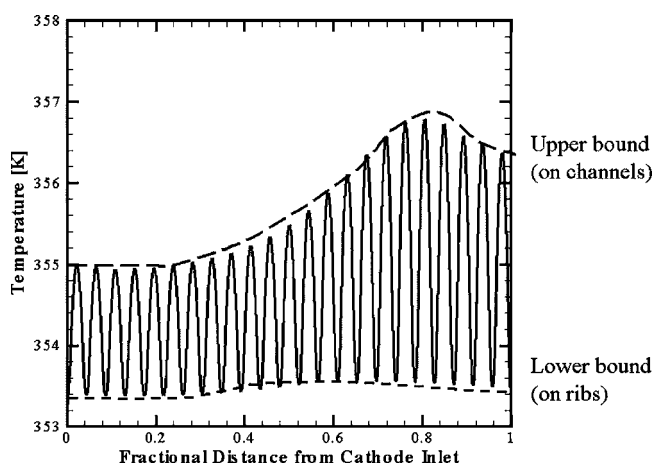


Figure 11. Temperature profile in the plane cutting across the middle of the fuel cell for case 2: $RH_a/RH_c = 75\%/0\%$ and $V_{cell} = 0.7$ V.

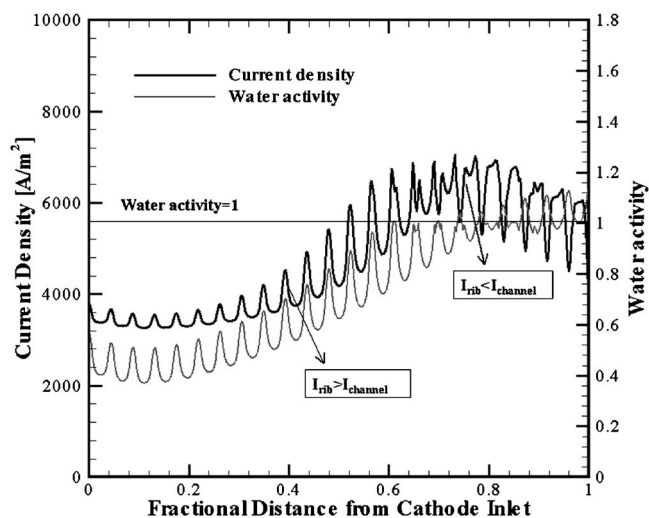


Figure 12. Current density and water activity profiles in the plane cutting across the middle of the fuel cell for case 2: $RH_a/RH_c = 75\%/0\%$ and $V_{cell} = 0.7$ V.

activity in the rib region is higher than in the channel area, because the temperature in the rib region is lower as described before. As a result, the current density in the rib region is greater than in the channel for roughly the first 60% of the cathode flow path, where the membrane is not fully hydrated and thus performance is mainly determined by the extent of membrane hydration. In contrast, near the outlet of the fuel cell where the membrane is almost fully humidified, the current density begins to be controlled by oxygen transport. The local current density becomes higher in the channel region than under the ribs because the ribs impose more severe oxygen transport limitation. In comparison, the current and water activity profiles for case 7 (*i.e.*, the fully humidified case) at 0.7 V are plotted in Fig. 13. The current density in the channel region is always higher than in the rib region, reiterating that the current density distribution is controlled by oxygen depletion in the 100% humidified case.

Table V presents an analysis of overall heat balance as well as

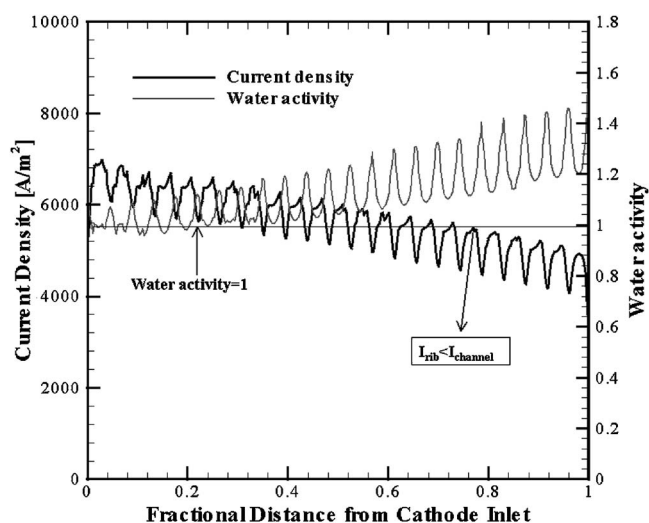


Figure 13. Current density and water activity profiles in the plane cutting across the middle of the fuel cell for case 7: $RH_a/RH_c = 100\%/100\%$ and $V_{cell} = 0.7$ V.

Table V. Summary of energy balance results ($A_{\text{react}} = 50 \text{ cm}^2$).

| Cell voltage, V_{cell} | | Case 2 (0.85 V) | Case 2 (0.75 V) | Case 2 (0.7 V) |
|--|--|--------------------|--------------------|--------------------|
| Average current density, I_{avg} , A/m ² | | 796 | 3201 | 4764 |
| Total heat released | Eq. 21, W | 2.47 | 11.16 | 17.51 |
| (1) Anode catalyst layer | Irreversible reaction heat, W: $S_{T,\text{irrev,a}} = \int vj \times \eta dV$ | 0.00725 (0.29%) | 0.1218 (1.09%) | 0.2747 (1.56%) |
| | Ohmic joule heating, W: $S_{T,\text{jouleH,a}} = \int vI^2 / \kappa^{\text{eff}} dV$ | 0.00539 (0.22%) | 0.0812 (0.73%) | 0.1857 (1.06%) |
| (2) Membrane | Ohmic joule heating, W: $S_{T,\text{jouleH,mem}} = \int vI^2 / \kappa^{\text{eff}} dV$ | 0.0432 (1.75%) | 0.4984 (4.45%) | 1.0692 (6.08%) |
| (3) Cathode catalyst layer | Irreversible reaction heat, W: $S_{T,\text{irrev,c}} = \int vj \times \eta dV$ | 1.1393 (46.13%) | 5.2600 (47.01%) | 8.1920 (46.57%) |
| | Ohmic joule heating, W: $S_{T,\text{jouleH,c}} = \int vI^2 / \kappa^{\text{eff}} dV$ | 0.0154 (0.62%) | 0.0442 (0.40%) | 0.0217 (0.12%) |
| | Entropic heat, W: $S_{T,\text{rev,c}} = \int vj \times (-T \partial U_o / \partial T) dV$ | 1.2624 (51.10%) | 5.0856 (45.45%) | 7.5802 (43.09%) |
| Sum | (1) + (2) + (3), W | 2.47 | 11.19 | 17.59 |
| Energy efficiency, η_e | Eq. 22 | 0.579 | 0.516 | 0.482 |

the individual heat sources for case 2 ($\text{RH}_a/\text{RH}_c = 75\%/0\%$) at 0.85, 0.75, and 0.7 V. The total heat released from the PEFC without phase change of water is given by

$$Q_{\text{total}} = \left(U_o - T \frac{\partial U_o}{\partial T} \right) \times I \times A_{\text{react}} - V_{\text{cell}} \times I \times A_{\text{react}} \quad [21]$$

where the first term on the right side of Eq. 21 is the maximum chemical power available from the overall H_2/O_2 reaction, and the second term is the electrical power produced by a fuel cell. The energy efficiency of the fuel cell, η_e , can thus be calculated from the ratio of these two terms, *i.e.*

$$\eta_e = \frac{V_{\text{cell}} \times I \times A_{\text{react}}}{\left(U_o - T \frac{\partial U_o}{\partial T} \right) \times I \times A_{\text{react}}} = \frac{V_{\text{cell}}}{U_o - T \frac{\partial U_o}{\partial T}} \quad [22]$$

Table V shows that the total sum of all heat sources computed from the 3D numerical model agrees very well with the overall heat generation rate calculated from the simple thermodynamic equation, Eq. 21. These energy balance calculations demonstrate the validity and accuracy of the present nonisothermal PEFC model. Furthermore, it is indicated in Table V that the most heat comes from the irreversible reaction and entropic heat sources in the cathode catalyst layer. In addition, the energy efficiency, η_e , is calculated and shown in Table V. The energy efficiencies for the cell voltages of 0.85, 0.75, and 0.7 V are ~ 58 , 52, and 48%, respectively.

Conclusions

The main focus of this study is to validate a three-dimensional, nonisothermal, PEFC model against the current distribution data experimentally measured under a wide variety of inlet humidification and cell voltage conditions. Major conclusions can be summarized as follows:

1. Good agreement between the simulation results and experimental measurements is achieved, validating the PEFC model at the detailed distribution level. However, the agreement becomes weaker at lower cell voltages. The deviation can be attributed to flooding by excess liquid water, which has not been accounted for in the present work.

2. Different shapes of current distribution are illustrated, depending on the inlet humidification conditions. Under fully humidified conditions, the local current density is controlled by concentration polarization and thus continuously decreases from the cell inlet to outlet. Low-humidity operation shows initially increasing current density as the membrane gains moisture from product water. When the membrane gets nearly fully hydrated, oxygen depletion effects

begin to control the current density distribution, showing decreasing current density toward the cell outlet. In addition, the thermal effect becomes more significant in the low-humidity operation, affecting the degree of membrane hydration and thus current distribution in PEFC. Therefore, water and thermal management strategies must be considered simultaneously and appropriately coordinated depending on the gas humidification conditions.

3. The membrane temperature is lower in the region facing the current collector rib. This fact exacerbates flooding by liquid water underneath the current collector ribs. Therefore, the GDL thermal conductivity plays an important role in coupling thermal and water management of PEFC.

4. The reversible reaction and entropic heats in the cathode catalyst layer are the major heat sources, releasing about 80-90% of the total waste heat.

Future work will include the validation of comprehensive CFCD models against distribution data of multiple parameters, such as current, species, and temperature distributions. This possibility is becoming a reality as new experimental techniques are emerging such as the simultaneous measurement of high-frequency resistance, current, and species (*e.g.*, water) distributions.²⁸ The validation of CFCD models against multiple arrays of distribution data will assist in developing a fuller understanding of PEFC fundamentals.

Acknowledgments

Funding for this work from W. L. Gore & Associates, Inc. is gratefully acknowledged. Thanks are also due to Mr. Qunlong Dong and Dr. Matthew Mench for useful discussions on the experimental data.

The Pennsylvania State University assisted in meeting the publication costs of this article.

List of Symbols

| | |
|-------|--|
| a | water activity |
| A | area, m ² |
| C | molar concentration, mol/m ³ |
| D | mass diffusivity of species, m ² /s |
| E_a | activation energy for oxygen reduction reaction in cathode side, J/mol |
| F | Faraday constant, 96 487 C/mol-e |
| i_0 | exchange current density, A/m ² |
| I | current density, A/m ² |
| j | transfer current, A/m ³ |
| k | thermal conductivity, W/mK |
| K | hydraulic permeability, m ² |
| p | pressure, Pa |
| n | number of electrons in electrochemical reaction |

| | |
|--------------------|---|
| n_d | electro-osmotic drag coefficient |
| Q_{total} | total heat released, W |
| R | the universal gas constant, 8.314 J/mol K |
| RH | relative humidity |
| s | stoichiometry coefficient in electrochemical reaction |
| S | source term in transport equation |
| T | temperature, K |
| \mathbf{u} | velocity vector, m/s |
| V_{cell} | cell potential, V |
| U_o | thermodynamic equilibrium potential, V |

Greek

| | |
|---------------------------|---|
| α | transfer coefficient |
| ε | volume fraction of gaseous phase in porous region |
| ε_{mc} | volume fraction of ionomer phase in catalyst layer |
| ϕ | phase potential, V |
| η | overpotential, V |
| η_e | energy efficiency |
| κ | ionic conductivity, S/m |
| λ | membrane water content, mol H ₂ O/mol SO ₃ ⁻ |
| μ | fluid viscosity, kg/m s |
| ρ | density, kg/m ³ |
| $\rho_{\text{dry,mem}}$ | dry membrane density, kg/m ³ |
| τ | tortuosity in porous region or viscous stress, N/m ² |
| ζ | stoichiometry flow ratio |

Superscripts

| | |
|-----|----------------------------------|
| e | electrolyte |
| eff | effective value in porous region |
| mem | membrane |
| g | gas |
| ref | reference value |
| sat | saturation value |

Subscripts

| | |
|----------------|----------------------------|
| a | anode |
| avg | average value |
| c | cathode |
| cat | catalyst |
| e | electrolyte |
| f | fluid |
| g | gas phase |
| GDL | gas diffusion layer |
| H ₂ | hydrogen |
| i | regions index |
| irrev | irreversible reaction heat |
| in | channel inlet |
| jouleH | joule heating |
| k | species index |
| mac | macro gas diffusion layer |

| | |
|----------------|--|
| mem | membrane |
| mic | micro gas diffusion layer |
| N ₂ | nitrogen |
| O ₂ | oxygen |
| react | electrochemical reaction |
| ref | reference value |
| rev | reversible reaction heat (entropic heat) |
| s | solid |
| sat | saturation value |
| T | energy equation |
| u | momentum equation |
| w | water |
| Φ | potential equation |
| 0 | standard condition, 298.15 K and 101.3 kPa (1 atm) |

References

- H. Ju and C. Y. Wang, *J. Electrochem. Soc.*, **151**, A1954 (2004).
- J. Newman, *Electrochemical Systems*, Prentice-Hall, Englewood Cliffs, NJ (1991).
- T. V. Nguyen and R. E. White, *J. Electrochem. Soc.*, **140**, 2178 (1993).
- J. S. Yi and T. V. Nguyen, *J. Electrochem. Soc.*, **145**, 1149 (1998).
- T. F. Fuller and J. Newman, *J. Electrochem. Soc.*, **140**, 1218 (1993).
- A. Rowe and X. Li, *J. Power Sources*, **102**, 82 (2001).
- S. Shimpalee and S. Dutta, *Numer. Heat Transfer, Part A*, **38**, 111 (2000).
- G. Maggio, V. Recupero, and C. Mantegazza, *J. Power Sources*, **62**, 167 (1996).
- P. Costamagna, *Chem. Eng. Sci.*, **56**, 323 (2001).
- T. Berning, D. M. Lu, and N. Djilali, *J. Power Sources*, **106**, 284 (2002).
- M. Wöhr, K. Bolwin, W. Schnurnberger, M. Fischer, and W. Neubrand, *Int. J. Hydrogen Energy*, **23**, 213 (1998).
- T. Zhou and H. Liu, *International Journal of Transport Phenomena*, **3**, 177 (2001).
- D. P. Wilkinson and J. St-Pierre, *J. Power Sources*, **113**, 101 (2003).
- L. Wang, A. Husar, T. Zhou, and H. Liu, *Int. J. Hydrogen Energy*, **28**, 1263 (2003).
- H. Ju, H. Meng, and C. Y. Wang, *Int. J. Heat Mass Transfer*, **48**, 1303 (2005).
- H. Meng and C. Y. Wang, *Chem. Eng. Sci.*, **59**, 3331 (2004).
- W. B. Gu and C. Y. Wang, *J. Electrochem. Soc.*, **147**, 2910 (2000).
- S. Um, C. Y. Wang, and K. S. Chen, *J. Electrochem. Soc.*, **147**, 4485 (2000).
- C. Berger, *Handbook of Fuel Cell Technology*, Prentice-Hall, Englewood Cliffs, NJ (1968).
- A. Parthasarathy, S. Srinivasan, and A. J. Appleby, *J. Electrochem. Soc.*, **139**, 2530 (1992).
- R. B. Bird, W. E. Stewart, and E. N. Lightfoot, *Transport Phenomena*, John Wiley & Sons, New York (1960).
- T. E. Springer, T. A. Zawodinski, and S. Gottesfeld, *J. Electrochem. Soc.*, **136**, 2334 (1991).
- R. E. Meredith and C. W. Tobias, in *Advances in Electrochemistry and Electrochemical Engineering 2*, C. W. Tobias, Editor, Interscience Publishers, New York (1962).
- M. M. Mench, Q. L. Dong, and C. Y. Wang, *J. Power Sources*, **124**, 90 (2003).
- Q. Dong, D. Shield, M. M. Mench, and U. Beuscher, *J. Electrochem. Soc.*, In press.
- STAR-CD Version 3.15 methodology, CD-Adapco Group (2001).
- J. Kolde, *2003 Fuel Cell Seminar*, Miami Beach, FL, November 2003.
- X. G. Yang, N. Burke, C. Y. Wang, K. Tajiri, and K. Shinohara, *J. Electrochem. Soc.*, **152**, A759 (2005).